Supplementary Information for

Crustal fingering facilitates free-gas methane migration through the hydrate stability zone

Xiaojing Fu, Joaquin Jimenez-Martinez, et al.

This PDF file includes:

Supplementary text
Figs. S1 to S7
Table S1
Captions for Movies S1 to S4
References for SI reference citations

Other supplementary materials for this manuscript include the following:

Movies S1 to S4

Supporting Information Text

Laboratory experiments

Observation of solid crust formation. During the depressurization phase, direct visualization of newly formed hydrate crust becomes challenging, but is apparent in certain regions where the gas-liquid interface appears rough. In addition, the formation of solid hydrate crust can be inferred indirectly. If solid hydrate formation does not take place, then the expansion of the single gas bubble is expected to be stable and uniform, analogous to that of balloon inflation. However, during the controlled depressurization, we do not observe stable expansion of gas into water (Fig. 2c). In fact, the gas volume remains unchanged for a few minutes while pressure decreases, suggesting that the gas phase is initially trapped by the pre-existing hydrate crust. The pressure difference between gas and liquid eventually builds up enough to rupture the hydrate crust (Fig. 2c, $t =$2.5min), allowing gas to displace into the ambient liquid. The consequent displacement pattern is finger-like, suggesting that a solid layer of hydrate along the gas-liquid interface is spontaneously forming and modulating the direction of gas flow.

Validation of hydrate formation. Here, we provide evidence that the observed solid that forms along gas fingers indeed represents gas hydrates:

1. **Control experiment with water and air bubble** under the same condition ($25°$C, ≤ 7.5MPa) does not show the formation of a solid around the gas bubble;

2. **Direct visual observation of hydrate dissociation.** When the pressure is within the hydrate stability zone, the roughness and jaggedness of the interface means that there is a solid forming (3, 4) (see also SI video 1 and Figure 2a). Once the pressure exits the stability zone, we observe that solid hydrate dissociation is two-staged. During the first stage, the solid crusts along fingers gradually disappear, showing hydrate melting into the surrounding liquid (Figure S2a). The dissociated hydrate leaves behind water that is supersaturated with xenon. During the second stage, the supersaturated solution undergoes spinodal decomposition, leading to exsolution of gas bubbles (Figure S2b).

Effect of subcooling on hydrate growth along the fingers. Subcooling (T_{eq}-T) plays an important role on the rate of hydrate growth and should control the pattern formation of crustal fingers. In particular, the rate of growth along the interface (R_s) is positively linked to the subcooling with a power law behavior (3). In our experiments, T_{eq}-T (the distance between the red arrow and the blue phase boundary in Figure 1b) is not fixed as we depressurize. Rather, it decreases with time (and pressure). Therefore, we should expect that crust that forms later in the experiment to grow slower and thus appears thinner. We illustrate this in Figure S3, where we show experimental snapshots at two different subcoolings: $\Delta T_1 \approx 11°C$ (at $t \approx 280s$) and $\Delta T_2 \approx 5°C$ (at $t \approx 1000s$). As expected, the thickness of the crust along the fingering front appears to be thinner at ΔT_2.

Phase-field modeling

We develop a continuum-scale phase-field model to study gas–liquid–hydrate systems far from thermodynamic equilibrium(5). We denote by ϕ_α the volumetric fractions of phase α, where $\alpha = g, l, s$ refers to the gas, liquid and hydrate phase, respectively. At any given point in the continuum domain they satisfy: $\phi_g + \phi_l + \phi_s \equiv 1$. The system is also characterized by the pointwise mole fraction of CH$_4$ or Xe: $\chi = N_{\text{CH}_4 \text{ or Xe}}/(N_{\text{CH}_4 \text{ or Xe}} + N_{\text{H}_2\text{O}})$.

Free energy design. We start by designing a simplified version of the Gibbs free energy functional for the three phase as a function of χ and temperature (T):

$$f_l(\chi,T) = \omega_{\text{mix}}\{\chi \log(\chi) - (1-\chi)\log(1-a_l(T)\chi)$$
$$- \chi \log(1-b_l(1-\chi)) + f_{l0}\}, \tag{1}$$

$$f_g(\chi,T) = \omega_{\text{mix}}\{\chi \log(\chi) - (1-\chi)\log(1-a_g\chi)$$
$$- \chi \log(1-b_g(T)(1-\chi)) + f_{g0}\}, \tag{2}$$

$$f_s(\chi,T) = \omega_{\text{mix}}\left\{a_s(T)(\chi-\chi_s)^2 + b_s(T) + f_{s0}\right\}, \tag{3}$$

where ω_{mix} [J/cm^3] is a characteristic energy density. We account for nonlinear temperature dependence of f_α as suggested by (6) for gas and liquid [Eqs. Eq. (1)–Eq. (2)], and as suggested by the solidification literature (7–9) for the solid phase [Eq. Eq. (3)]: $a_l = a_{l0}/(T/T_c)^4$, $b_g = b_{g0}/(T/T_c)^2$, $a_s = a_{s0}(T/T_c)$ and $b_s = b_{s0}(T/T_c)$, where $T_c = 1$K is the scaling temperature.

Under the phase-field framework, the f_α's are incorporated into the total free energy $F(\chi,\boldsymbol{\phi},T)$, which also considers the energetic interactions between phases, and is composed of the bulk free energy f_0 and the interfacial energy (gradient squared terms):

$$F = \int_V \left[f_0(\chi,\boldsymbol{\phi},T) + \epsilon_c^2(T)|\nabla\chi|^2 \right.$$
$$+ \epsilon_{gl}^2(T)\nabla\phi_g \cdot \nabla\phi_l + \epsilon_{gs}^2(T)\nabla\phi_g \cdot \nabla\phi_s$$
$$+ \epsilon_{sl}^2(T)\nabla\phi_s \cdot \nabla\phi_l + \epsilon_g^2(T)|\nabla\phi_g|^2$$
$$\left. + \epsilon_l^2(T)|\nabla\phi_l|^2 + \epsilon_s^2(T)|\nabla\phi_s|^2 \right]dV. \tag{4}$$

Xiaojing Fu, Joaquin Jimenez-Martinez, et al.

A detailed description of f_0 in F and its parameters for CH$_4$ and Xe hydrates can be found in (2, 5). By calibrating the parameters in the above energy (CH$_4$ parameters reported in Extended Table S1), we can recover the isobaric temperature–composition phase diagram predicted by existing thermodynamic equilibrium predictions (Fig.S4).

Evolution equations. The proposed free energy F is incorporated into a phase-field model to study the nonequilibrium thermodynamics of the three-phase system. The evolution of the system variables (χ and ϕ_α's) is driven by potentials Ψ, which are variational derivatives of F:

$$\Psi_\chi = \frac{\partial F}{\partial \chi} - \nabla \cdot \frac{\partial F}{\partial \nabla \chi}, \tag{5}$$

$$\Psi_{\phi_\alpha} = \frac{\partial F}{\partial \phi_\alpha} - \nabla \cdot \frac{\partial F}{\partial \nabla \phi_\alpha}, \quad \alpha = g, l, s. \tag{6}$$

To describe the evolution dynamics, we start by imposing mass conservation of the total mixture (methane plus water):

$$\frac{\partial \rho}{\partial t} + \nabla \cdot (\rho \mathbf{u}) = 0. \tag{7}$$

Additionally, we prescribe the conservation of mass of methane using a Cahn-Hilliard-type equation for χ:

$$\frac{\partial \rho \chi}{\partial t} + \nabla \cdot (\rho \chi \mathbf{u}) - R_\chi \nabla \cdot \left(D(\{\phi_\alpha\}) \rho \nabla \Psi_c \right) = 0. \tag{8}$$

We complete the system with a non-conserved Allen-Cahn evolution equation for ϕ_g and ϕ_s in an advective form:

$$\frac{\partial \phi_\alpha}{\partial t} + \mathbf{u} \cdot \nabla \phi_\alpha + R_\phi \Psi_\alpha = 0. \tag{9}$$

Here, R_χ is the effective rate of diffusion and $D(\boldsymbol{\phi}) = \phi_g D_g + \phi_l D_l + \phi_s D_s$ is a dimensionless mixture diffusion coefficient (where D_g, D_l and D_s are normalized by a characteristic gas-phase diffusion coefficient D_{gas}). We adopt $D_g = 1$, $D_l = 10^{-3}$ and $D_s = 10^{-11}$ (whose relative magnitudes are consistent with experimental measurements (10, 11) and emulate slow diffusion in liquid and extremely slow diffusion within hydrate). R_{ϕ_α} in Eq. 9 is the rate of phase change for phase α. We assume isothermal conditions in our model.

Multiphase Hele-Shaw flow. We assume that flow occurs predominantly parallel to the glass plates at low Reynolds number, which allows us to simplify the flow description using the Hele-Shaw approximation (12). Instead of identifying and tracking velocities within each phase, we assume a mixture velocity (at each point in the domain) that obeys Darcy's law:

$$\mathbf{u}(x, y) = \frac{-k}{\mu(\phi_g, \phi_l, \phi_s)} \nabla p. \tag{10}$$

Gas compressibility is prescribed through a gas density that is linearly dependent on pressure. Here we simplify our description of phase compressibility by imposing a linear pressure dependence in density for all three phases:

$$\rho_\alpha = \rho_{\alpha 0} + c_t^\alpha p. \tag{11}$$

Finally, it is convenient for modeling to define a mixture density, which is the mass per volume at a given point in the domain. Here we describe the mixture density as a ϕ_α-weighted average:

$$\rho = \rho_l \phi_l + \rho_g \phi_g + \rho_s \phi_s. \tag{12}$$

We model all three phases as fluid with a certain viscosity. Specifically, we assume that the hydrate phase is the most viscous and gas the least viscous phase. We assume that the viscosities of all phases are independent of composition and normalize the values by the liquid water viscosity μ_{water} so that:

$$\mu_g = 1/M, \quad \mu_l = 1, \quad \mu_s = M. \tag{}$$

We define a mixture viscosity by blending the three viscosities by a phase-weighted average:

$$\mu(\{\phi_\alpha\}) = \mu_{\text{water}}(\mu_g \phi_g + \mu_l \phi_l + \mu_s \phi_s), \tag{13}$$

similar to what is done to diffusion coefficients in Eq. Eq. (8).

The hydrate phase is described as an extremely viscous fluid, whose viscosity also hardens (increases) with its age:

$$\frac{d\theta}{dt} = \phi_s \left(r - \frac{|\mathbf{u}|\theta}{D} \right), \tag{14}$$

$$\mu_s = \theta \mu_{s0}. \tag{15}$$

We introduce some variability in the hydrate growth rate along the initial gas-liquid interface, which creates a thinner segment along the crust that is prone to be broken through.

Numerical simulations

To understand how hydrate grows on a quiescent interface, we first perform a series of simulations in 1D. The left portion of the domain is filled with gas and the other portion filled with gas-saturated liquid water (Fig. S5a). The model successfully simulates the nucleation and growth of hydrate on the initially hydrate-free gas-liquid interface (Fig. S5b). By analyzing the growth dynamics, we find that the parameter R_s controls the rate at which hydrate grows towards its finite thickness (Fig. S5b). However, the nonequilibrium steady-state thickness of hydrate is independent of the rate of hydrate formation (R_s) (Fig. S5b).

A. Gas escaping from crusted bubble.. These simulations (Fig. 3a-b) are performed in a domain (rectangular or square) initially filled with partially saturated liquid and a single gas bubble with pre-existing crust. The ambient liquid is withdrawn from the upper left corner at a constant rate Q_{outlet} (Fig. S6a). After breaking away from the pre-existing crust, gas flows within a single hydrate-crusted finger channel towards the fluid outlet (see Supplementary Video 3). The resistance to flow provided by the crust allows for flow focusing within a thin channel. The meandering behavior of the gas finger is mainly due to flow resistance by the crust. However, the imposed permeability heterogeneity (Fig. S6b) also plays a role in the randomness of the pattern.

B. Field-scale simulations.. Assuming that the bottom simulating reflector (BSR)— the interface between an underlying gas reservoir and its overlying sediments— is initially flat and a hydrate layer readily forms (Extended Fig .S7), we then supply methane gas to the gas reservoir through periodic recharge events with an interval of $1/f$ and a maximum flow rate of Q_{in} (Fig. S6a). After each recharge events, we assume an exponential decay of reservoir pressure with time, and thus an exponentially decaying profile for the gas flux at the bottom boundary. The BSR is seeded with seven locations that are prone to gas breakthrough. This is achieved by assuming $R_s = 0$ at these locations so that hydrate does not form locally. In practice, these could be local weak spots formed by hydrofracturing of the hydrate-bearing permeability seal (13), roughness of the BSR (14) or coupled fluid flow and solid deformation that leads to decompaction weakening (15). The simulations can be viewed in Supplementary Video 4.

Xiaojing Fu, Joaquin Jimenez-Martinez, et al.
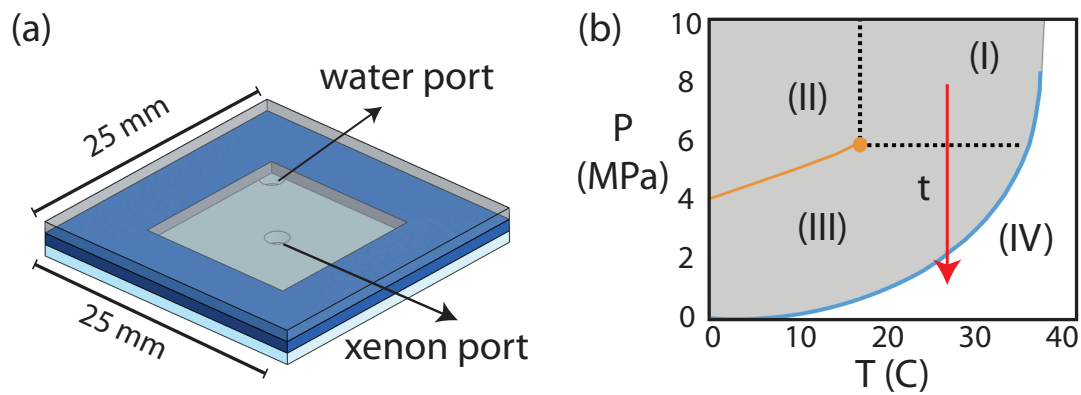
Fig. S1. Experimental setup. a, Birds eye view of the microfluidic flow cell with dimensions. The gap thickness is 1 mm. **b,** P-T phase diagram for Xe-H_2O systems, indicating coexistence of hydrate with supercritical Xe (I), hydrate with liquid Xe (II), hydrate with gaseous Xe (III) and liquid water with gaseous Xe (IV). The red arrow indicates the trajectory imposed during experiments in the microfluidic cell.
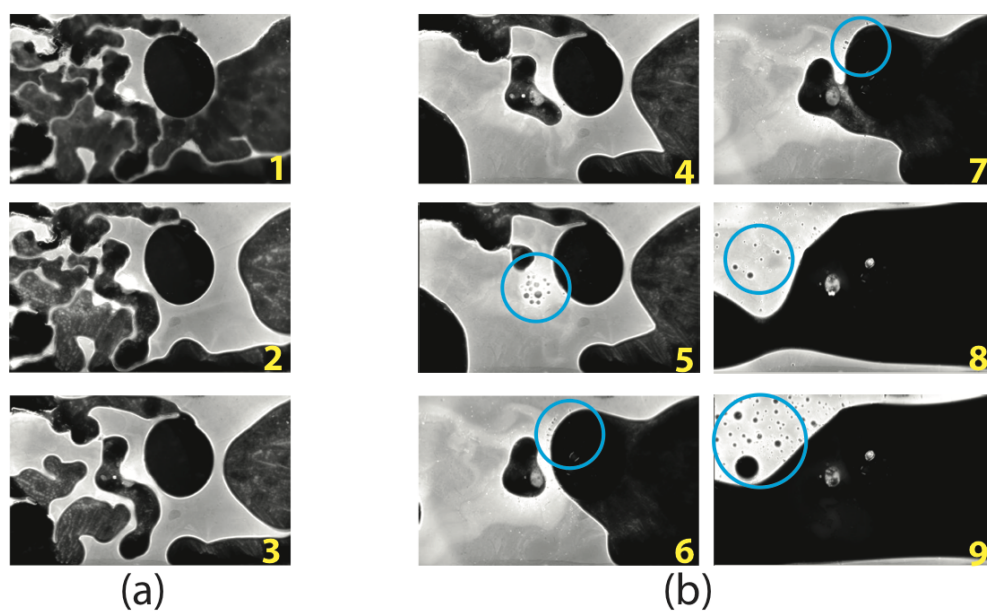
Fig. S2. Direct visual observation of gas hydrate dissociation in two stages of the experiment. Yellow numbers correspond to time sequence. (a) First stage: hydrate crust melts into the surrounding liquid, creating an aqueous solution supersaturated in xenon; (b) second stage: the supersaturated solution undergoes spinodal decomposition, creating many xenon gas bubbles (blue circles mark regions of gas exsolution).

Xiaojing Fu, Joaquin Jimenez-Martinez, et al.
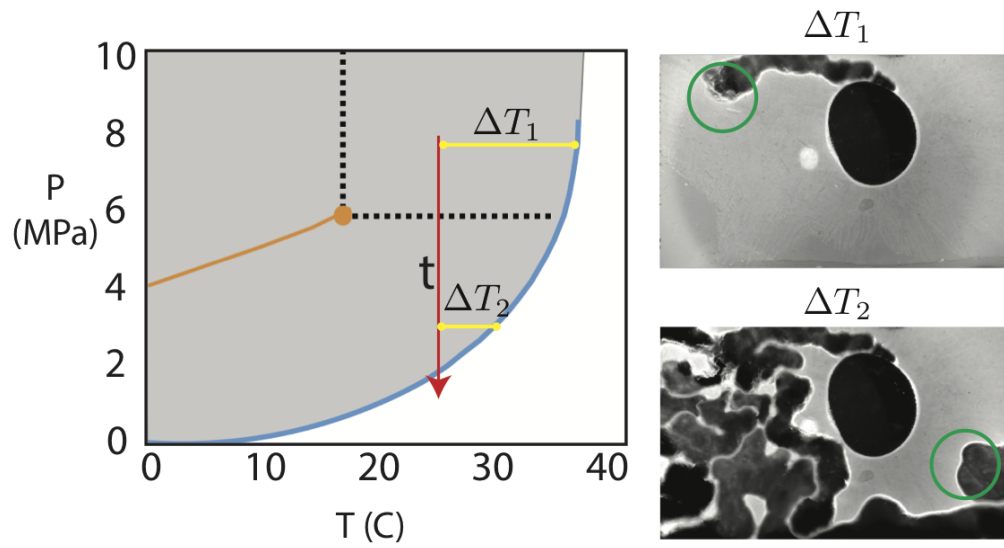
Fig. S3. (Left) P-T phase diagram for Xe-H_2O systems. The red arrow indicates the trajectory imposed during our experiments in the microfluidic cell. The yellow horizontal bars measure the subcooling at two different times during the experiment. (Right) The experimental snapshots corresponding to the two subcoolings in the left figure. Green circles mark the fingering front at the time the images are taken.
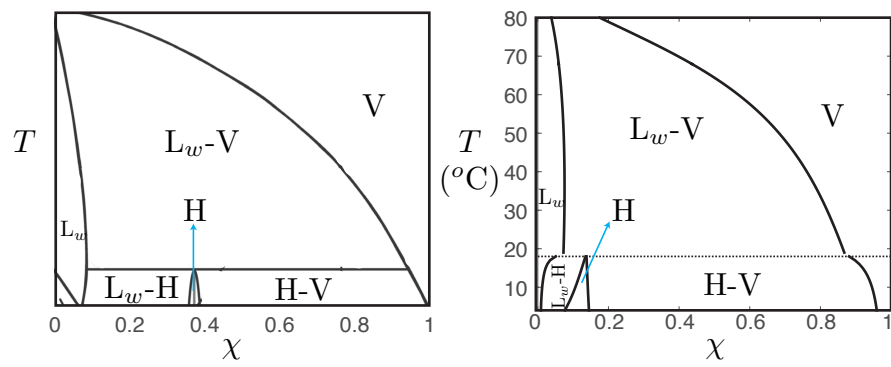
Fig. S4. Thermodynamic phase diagram. The isobaric phase diagram for CH_4 and H_2O calculated by (left) CSMGem and (right) our model.
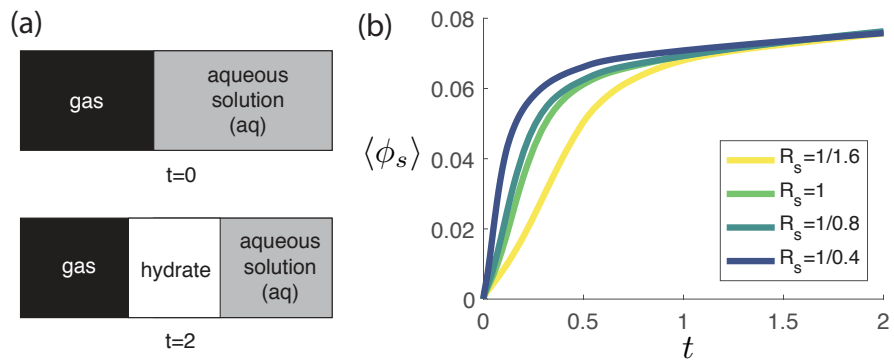
Fig. S5. Hydrate growth on a quiescent interface. a, Diagram illustrating the interfacial hydrate growth problem. **b,** The thickness of interfacial hydrate as a function of time for different growth rates (R_s), calculated by 1D simulations of our model on the problem illustrated in **a**.
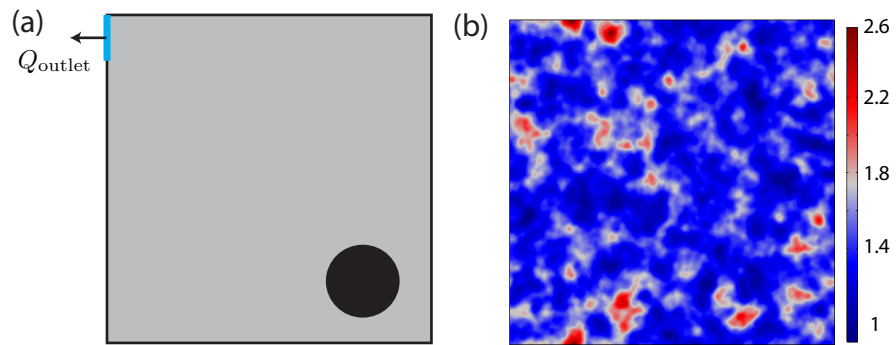
Fig. S6. Setup for pore-scale simulations. a, In a square domain, the gas bubble is initially placed at the lower right corner and liquid withdrawn from the upper left corner. **b,** Imposed heterogenous permeability field that introduces randomness to the meandering pattern.
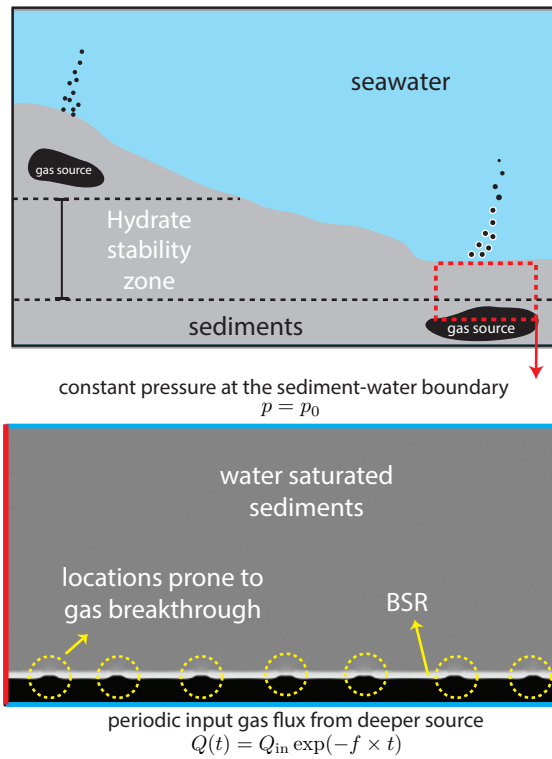
Fig. S7. Initial condition of the field-scale simulations. The bottom figure is the enlarged portion marked by the red dashed box in the top figure. In the bottom figure, the yellow dashed circles indicate locations prone to gas breakthrough along the gas-water interface (BSR). These locations are artificially seeded by imposing locally a much lower rate of hydrate formation (R_s). A no-flow condition is imposed at the left and right boundaries. A constant pressure is imposed at the top boundary (sediment-water interface). A periodic input gas flux is imposed uniformly along the bottom boundary.

Table S1. Parameters used for Gibbs free energy calculations for methane and xenon systems.

P	a_g	b_{g0}	f_{g0}	a_{l0}	b_l	f_{l0}	a_{s0}	χ_s	b_{s0}	f_{s0}
7.5MPa	0.1	-1×10^{10}	-6	-1×10^{10}	0.1	-2	6500	0.146	0.65	-63

Xiaojing Fu, Joaquin Jimenez-Martinez, et al.

Movie S1. Supplementary video 1: Growth of hydrate crust on the gas-liquid interface of a bubble placed within a Hele-Shaw cell.

Movie S2. Supplementary video 2: Experimental observation of crustal fingering.

Movie S3. Supplementary video 3: Comparison between experiments and simulations.

Movie S4. Supplementary video 4: Field-scale simulations illustrating formation of gas conduits and pockets.

References

1. Porter ML, et al. (2015) Geo-material microfluidics at reservoir conditions for subsurface energy resource applications. *Lab Chip* 15(20):4044–4053.
2. Fu X, Waite WF, Cueto-Felgueroso L, Juanes R (2019) Xenon hydrate as an analogue of methane hydrate in geologic systems out of thermodynamic equilibrium. *Geochem. Geophys. Geosyst.* 20:2462–2472.
3. Touil A, Broseta D, Desmedt A (2019) Gas hydrate crystallization in thin glass capillaries: roles of supercooling and wettability. *Langmuir* 35:12569–12581.
4. Atig D, Broseta D, Pereira JM, Brown R (2020) Contactless probing of polycrystalline methane hydrate at pore scale suggests weaker tensile properties than thought. *Nat. Comm.* 11:3379.
5. Fu X, Cueto-Felgueroso L, Juanes R (2018) Nonequilibrium thermodynamics of hydrate growth on a gas a liquid interface. *Phys. Rev. Lett.* 120(14):144501.
6. Wilson G (1964) A new expression for the excess free energy of mixing. *J. Am. Chem. Soc.* 86(2):127–130.
7. Nestler B, Wheeler AA, Ratke L, Stöcker C (2000) Phase-field model for solidification of a monotectic alloy with convection. *Physica D* 141:133–154.
8. Moelans N (2011) A quantitative and thermodynamically consistent phase-field interpolation function for multi-phase systems. *Acta Mater.* 59(3):1077–1086.
9. Cogswell DA, Carter WC (2011) Thermodynamic phase-field model for microstructure with multiple components and phases: The possibility of metastable phases. *Phys. Rev. E* 83(6):061602.
10. Witherspoon PA, Saraf DN (1965) Diffusion of Methane, Ethane, Propane, and n-Butane. *J. Phys. Chem.* 69(11):3752–3755.
11. Peters B, Zimmermann NER, Beckham GT, Tester JW, Trout BL (2008) Path sampling calculation of methane diffusivity in natural gas hydrates from a water-vacancy assisted mechanism. *J. Am. Chem. Soc.* 130(51):17342–17350.
12. Cueto-Felgueroso L, Juanes R (2014) A phase-field model of two-phase Hele-Shaw flow. *J. Fluid Mech.* 758:522–552.
13. Nimblett J, Ruppel C (2003) Permeability evolution during the formation of gas hydrates in marine sediments. *J. Geophys. Res.* 108(B9):2420.
14. Wood WT, Gettrust JF, Chapman NR, Spence GD, Hyndman RD (2002) Decreased stability of methane hydrates in marine sediments owing to phase-boundary roughness. *Nature* 420(6916):656–660.
15. Räss L, Simon NSC, Podladchikov YY (2018) Spontaneous formation of fluid escape pipes from subsurface reservoirs. *Sci. Rep.* 8:11116.